Supplemental Materials

Molecular Biology of the Cell

Backlund et al.

SUPPORTING MATERIAL

Correlations of three-dimensional motion of chromosomal loci in yeast revealed by the Double-Helix Point Spread Function microscope

Mikael P. Backlund[a], Ryan Joyner[b], Karsten Weis[b, c], and W. E. Moerner[a]

[a]Department of Chemistry, Stanford University

[b]Department of Cell and Developmental Biology, University of California, Berkeley

[c]Institute of Biochemistry, Department of Biology, ETH Zürich, 8093 Zürich, Switzerland

TABLE OF CONTENTS:

A. Empirical correction for *z*-dependent registration error

As explained in the Materials and Methods section, the 3D transformation map from red coordinates into green coordinates was found by scanning a sample of beads immobilized at the coverslip throughout a 3D volume. However, since the loci to which we applied the transformation were distributed at various distances from the coverslip, at various depths into the mismatched medium, one might expect a residual *z*-dependent registration error. Our GFP-crosstalk sample provided a means to assess such an error, since the signal in both channels marked the same object. Figure S1 shows the residual *x*, *y*, and *z* registration error (green minus red) from this crosstalk data as a function of apparent *z* position in the red channel. Each point represents a measurement from one frame of one track pair. If there were no residual *z*-dependent error due to the depth into the mismatched medium, each of these plots would be a flat horizontal line centered at 0 error, with some spread due to unbiased error. By contrast, the distinct curvature present in the plots (especially in *z*) reveals a bias that should be removed. To correct this we fit each of the plots to a piecewise sum of low order polynomials, then applied the resulting average correction to each localization in conjunction with the original transformation function. We applied the same correction to data in each condition studied, despite the fact that the proper correction likely differs somewhat for each sample and each day's unique transformation function. Thus there may still be a small residual *z*-dependent error for the other conditions, but it is difficult to distinguish error from true locus separation in the cases where different objects were tagged in the two colors. After this correction, the error in the crosstalk data was improved such that the mean Euclidean distance between registered crosstalk loci (as calculated over the full duration of the tracks) went from 75 nm to 61 nm. Using the localization precisions estimated for the crosstalk experiments elsewhere in the Supporting Material, we would expect an average Euclidean distance of 57 nm in the absence of any bias, and so the corrected experimental value is consistent with removal of the bias. The Euclidean distance quoted in the main text (i.e. 48 nm) is lower because this number was calculated from only the first 10 frames of each track. Signal-to-noise is higher in these early frames, thus the contribution of localization error to the apparent inter-locus distance is lower.

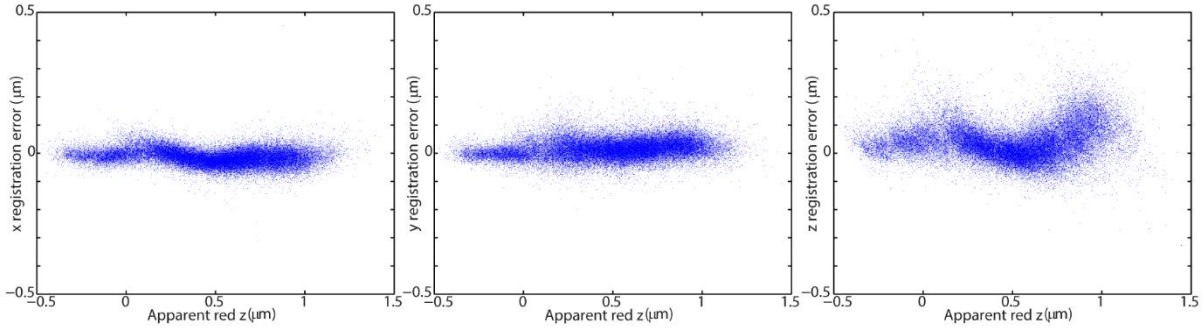

Figure S1 Residual registration error (green position minus red position) after transformation in *x*, *y*, and *z* from the pooled crosstalk data.

Strain #	Genotype	Source
KWY 3915	*MATα ybr022w::112TetO::URA3 leu2::TetR-3XmCherry::LEU2*	This Study
KWY 3926 (Crosstalk)	*MATa ybr022w::256LacO::LEU2 his3::LacI-GFP::HIS3*	This Study
KWY 3940 (DLDC)	*MATa/α his3::LacI-GFP::HIS3/his3Δ1 leu2Δ0/leu2::TetR-3XmCherry::LEU2 ybr022w::256LacO::LEU2/ybr022w::112TetO::URA3*	This Study
KWY 4339 (*GAL*/*PES4*)	*MATa/α his3::LacI-GFP::HIS3/his3Δ1 leu2Δ0/leu2::TetR-3XmCherry::LEU2 YBR022W/ybr022w::112TetO::URA3 yfr023w::256LacO::LEU2 /YFR023W*	This Study
KWY 5064 (*GAL*/*RPL9A*)	*MATa/α his3::LacI-GFP::HIS3/his3Δ1 leu2Δ0/leu2::TetR-3XmCherry::LEU2 YBR022W/ybr022w::112TetO::URA3 ygl147c::256LacO::LEU2 /YGL147C*	This Study
KWY 4087 (DLSC-30)	*MATa/α ybr022w::112TetO::URA3/YBR022W his3::LacI-GFP_TetR-3XmCherry::HIS3/his3Δ1 ybr028c::256LacO::LEU2/YBR028C*	This Study
KWY 4772 (DLSC-108)	*MATa/α ybr022w::112TetO::URA3/YBR022W his3::LacI-GFP_TetR-3XmCherry::HIS3/his3Δ1 ybr067c::256LacO::LEU2/YBR067C*	This Study

Table S1 Yeast strains used in this study. All strains are of the S288c (BY4743) background with genotype: *MAT*a/*α his3Δ1/his3Δ1 leu2Δ0/leu2Δ0 LYS2/lys2Δ0 met15Δ0/MET15 ura3Δ0/ura3Δ0.*

B. Slight bias due to crosstalk

The fact that we were able to fit the crosstalk signal of GFP in the red channel in the absence of mCherry means that some amount of crosstalk signal was present during our dual-color experiments. To minimize the effects of this, we preceded and succeeded every dual-color acquisition by imaging with only the 488nm laser on to provide an estimate of the amount of crosstalk relative to the mCherry signal for each imaged cell. In general, at the beginning of the dual-color acquisition the mCherry signal easily drowned out the crosstalk, while at the end of the acquisition it was either still much greater or comparable. For this reason, all inter-locus distances reported in this study were calculated from the first ten frames of each track pair. If the crosstalk level was obviously comparable to the mCherry signal at some point during the track we either threw the track out or truncated the analyzed track early. Also, if the crosstalk caused a large jump in the estimated position at a certain point during the track when the mCherry became sufficiently dim, this was noticeable in the manual filtering step (see Materials and Methods) and the track was truncated or discarded.

Despite these filters, it is possible that more subtle artifacts could arise as a result of the crosstalk. In particular, one can reason that strong enough crosstalk could cause a position estimation bias of the red locus toward the green locus, which could falsely inflate the calculated values for $C_v^{(g,r)}$. To assess the prevalence of such an effect we conducted simulations of correlated track pairs (see simulation section of Supporting Material) using experimental levels of signal, noise, and crosstalk. Each simulated track had $\alpha = 0.75$ and $D^* = 0.0021$. Simulations were carried out in 1D for simplicity. We adjusted the level of track pair correlation by choosing the parameter γ between 0 and 0.9 at intervals of 0.1 (see simulation section of Supporting Material for explanation of γ). For each γ we simulated 100 track pairs. Upon simulating each underlying track pair trajectory, we generated a sequence of noisy 1D "images" to be fit to produce estimated trajectories which could then be compared to the underlying values. Each "image" consisted of a carefully scaled Gaussian function of standard deviation 1.5 pixels (~190 nm) centered at the particle's underlying position, plus a constant background offset. A second scaled Gaussian function was added to the "red" image to mimic crosstalk. Noise was added to each "image" as a Gaussian random variable with variance twice its mean, in line with the statistics of EMCCD cameras operating at high gain levels (Hirsch *et al.*, 2013).

The amplitudes of each Gaussian and the level of background were chosen based on experimental parameters. In one set of simulations we chose the first DLDC-dextrose set of data to inform these levels. For each track pair from the experimental set we estimated the background level in each channel as a function of time by finding the median pixel value in a region around the DH-PSF in the raw data. This function was smoothed by fitting to a double exponential (to account for mCherry and GFP crosstalk bleaching) in the red channel, and by using a boxcar average in the green channel. We then estimated the signal in both channels by finding the maximum pixel value in each frame within a small box around the DH-PSF then subtracting the estimated background. The signal function was smoothed by fitting to an exponential function in the red channel, and by using a boxcar average in the green channel. We then estimated the crosstalk signal level at the beginning of the dual-color acquisition by taking the mean of the maximum pixel value in the frames prior to turning on the 561 nm laser. To estimate the crosstalk signal during the dual-color acquisition one could conceivably estimate the final crosstalk signal level by proceeding similarly in the frames after the 561 nm laser was turned off, then interpolating between the initial and final values. This was not done, however, since the crosstalk signal was often not easily perceptible at the end of the acquisition and so the maximum pixel value was not a good proxy for the signal. Instead we estimated the crosstalk background before and after the 561 nm laser was on by taking median pixel values within a specified region, then interpolated these initial and final values with an exponential function of a calculated time constant. We then assumed that the crosstalk signal bleached with the same time constant as the crosstalk background to produce an estimate for the crosstalk signal in each frame during the dual-color acquisition. This procedure generated a library of 53 sets of green signal, green background, red signal, red background, and crosstalk signal of some particular track length. We repeated the procedure using the data from the second DLDC-galactose set to create another library of 73 such sets capturing somewhat different photophysical behavior. We note that this procedure for emulating the photophysics was not perfect, as it seemed to predict somewhat larger localization errors in the dextrose case compared to galactose in the red channel, the opposite trend of what was determined for the experimental data (see Section C). This fact likely contributed to the larger spread in the simulated correlations for dextrose seen in Figure S2.

The track length and photophysical behavior to be assigned to each of the 100 simulated track pairs for each γ was chosen randomly (with replacement) from the library. The whole simulation consisting of 100 track pairs for each γ was repeated in 7 trials for the DLDC-dextrose library and 6 trials for the DLDC-galactose library. The results are shown in Figure S2, for both the DLDC-dextrose photophysics (Figure S2A) and the DLDC-galactose photophysics (Figure S2B). The plots show the difference between the estimated $C_v^{(g,r)}$ in the presence of crosstalk and the underlying true $C_v^{(g,r)}$, as a function of true $C_v^{(g,r)}$. Here $C_v^{(g,r)}$ was calculated for δ = 5 s and τ = 0. For comparison we also illustrate the effect of noise alone (i.e. no crosstalk signal added) on the estimated value of $C_v^{(g,r)}$. As expected, adding noise to the measurements deflates the estimate of $C_v^{(g,r)}$, increasingly so for larger true $C_v^{(g,r)}$. Adding crosstalk signal spreads the distribution of estimates and causes a small bias of < 0.05 for small true $C_v^{(g,r)}$. As true $C_v^{(g,r)}$ increases, the estimates in the presence of crosstalk converge to the line of noisy estimates. The take-home message from this simulation study is that while crosstalk may have caused slight inflation of our estimated $C_v^{(g,r)}$ in some cases, it likely cannot explain our main conclusions. Namely it does not seem to explain the differences among the conditions we studied, in part since it should preferentially inflate the cases with lower correlations, which would only slightly decrease the apparent gap between DLDC-dextrose and DLDC-galactose, unless there was a strong differential bias between the two conditions. This simulation is somewhat conservative as well since it assumes no correlation between inter-locus distance and $C_v^{(g,r)}$. In reality, loci with less correlated motions also tend to be further apart, which means that any crosstalk signal likely will confuse the red signal less often, which would reduce the bias in estimated $C_v^{(g,r)}$.

Comparison of Figure S2, A and B does predict that one could conceivably get a larger bias in the DLDC-dextrose case than in the DLDC-galactose case due to slightly different photophysics, which could contribute to the observed difference in mean correlations. To ensure that this possible contribution is not the main source of discrepancy, we also calculated the biases for the same simulated data, but limited the contributing track pairs to those exhibiting inter-locus distance either greater than or less than the ensemble mean starting distance. In the 1D simulation this amounted to calculating ensemble correlations only for tracks with R < ~350 nm (Figure S2, C and D), or R> ~350 nm (Figure S2, E and F). As can be seen, when we limit to loci

that are near each other, the bias becomes more pronounced and the apparent difference between DLDC-dextrose and DLDC-galactose becomes larger. When we limit to loci that are further apart, the bias is removed. In fact, because addition of noise from the crosstalk decreases the SNR, we see that the calculated cross-correlations actually become diminished. Most importantly, the difference between the DLDC-dextrose and DLDC-galactose correlations decreases (and even reverses sign in this simulation). This gives us an excellent benchmark to which to compare—if in our real data the difference in correlations becomes larger when we limit to loci which are nearer to one another than the mean inter-locus distance (~750 nm in 3D), and likewise this difference becomes smaller for further apart loci, then it is more difficult to rule out the crosstalk artifact as a major contributor to the observed effect. However, (at $\tau = 0$, $\delta = 5$ s) our data shows that limiting R > 750 nm gives T-EAVCC values of 0.19 for DLDC-dextrose and 0.04 for DLDC-galactose, while limiting to R< 750 nm gives 0.33 for DLDC-dextrose and 0.25 for DLDC-galactose. The difference in correlations is actually more pronounced for far-apart loci.

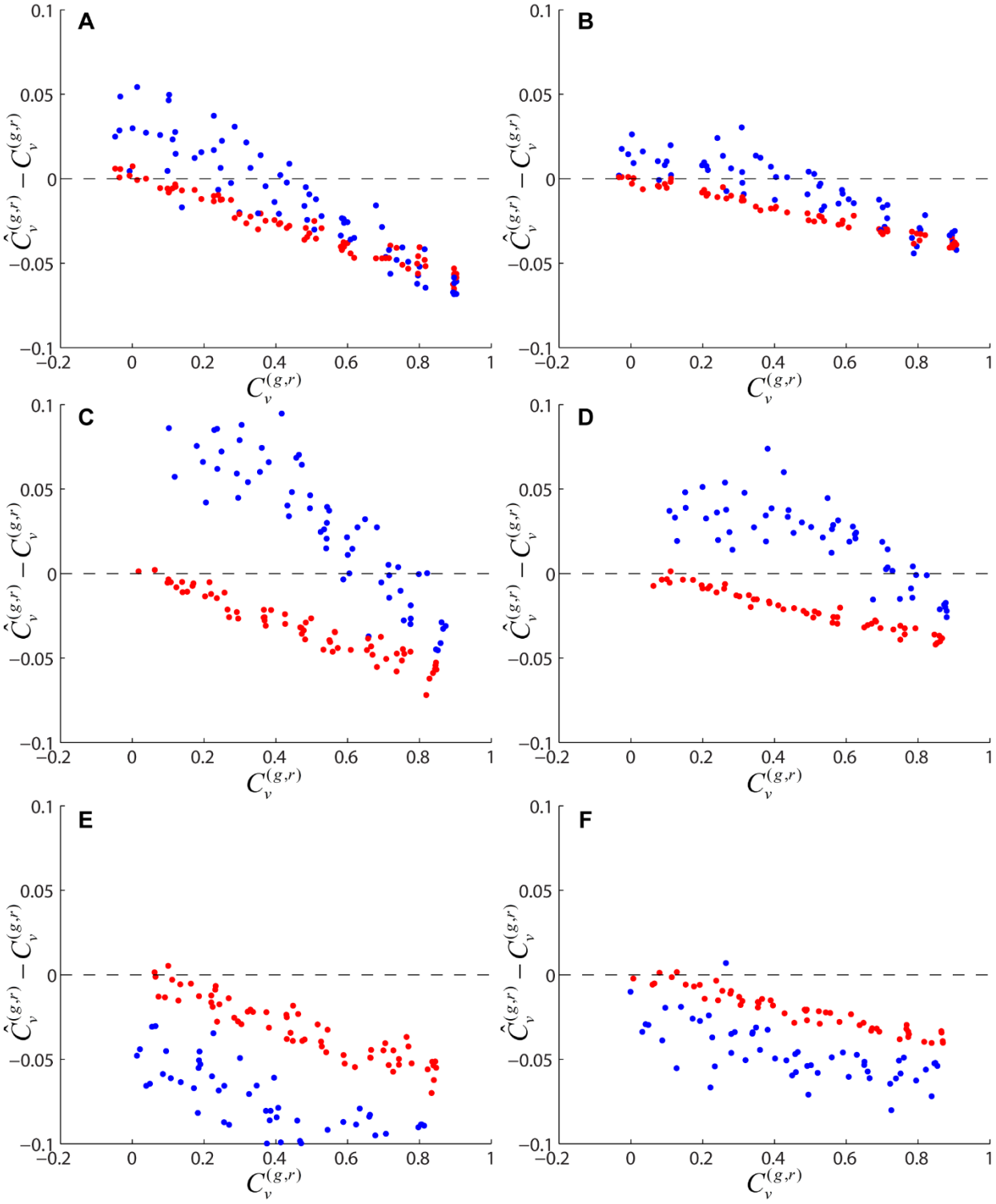

Figure S2 Differences between estimated time-ensemble averaged velocity-cross correlations and true values for simulations described in accompanying text. Here $C_v^{(g,r)}$ was calculated for δ = 5 s and τ = 0. Blue dots correspond to noisy estimates in the presence of crosstalk signal, while red dots correspond to noisy estimates in the absence of

crosstalk signal. Each dot represents an average over 100 track pairs generated for a single trial with a single value of γ. (A) Simulation generated using photophysical parameters from DLDC-dextrose set 1. (B) Simulation generated using photophysical parameters from DLDC-galactose set 2. (C) Same as (A) but limited to loci that are <350 nm apart. (D) Same as (B) but limited to loci that are <350 nm apart. (E) Same as (A) but limited to loci that are >350 nm apart. (F) Same as (B) but limited to loci that are >350 nm apart.

C. Estimation of localization precision

As mentioned in the main text, we estimated localization error in each dimension by tracing a straight line through the first two points in the 1D MSD and finding the intercept b. The localization precision is then related to b by Equation 1 (see main text). Equation 1 is a well-known relation (Savin and Doyle, 2005); however, it only strictly holds for pure Brownian motion. Since we show that the motion we observed in this study was not pure Brownian motion, Equation 1 represents an approximation. To assess the quality of this approximation for our purposes we simulated 3D fractional Brownian motion, as described in the simulation section of the Supporting Material, using subdiffusive parameters $D^* = 0.0020$ and $\alpha = 0.7$. We simulated 100 tracks each consisting of 300 steps spaced by 0.1 s. To account for motion blur we simulated each trajectory over 3000 microsteps separated by 0.01 s then averaged every 10 microsteps together to give the final 300 "measured" steps. We added localization error to each resulting 1D trajectory by adding a mean-zero Gaussian random vector of prescribed standard deviation to each dimension. First we used errors on the order of our estimates for the green channel throughout our experiments: $[\sigma_x, \sigma_y, \sigma_z] = [12\text{ nm}, 12\text{ nm}, 22\text{ nm}]$. We then applied our localization error estimation technique to the resulting simulated data, yielding estimates of $[\hat{\sigma}_x, \hat{\sigma}_y, \hat{\sigma}_z] = [14\text{ nm}, 14\text{ nm}, 23\text{ nm}]$. We repeated the simulation but used localization precision values on the order estimated for the red channel: $[\sigma_x, \sigma_y, \sigma_z] = [23\text{ nm}, 27\text{ nm}, 41\text{ nm}]$, which led to estimates of $[\hat{\sigma}_x, \hat{\sigma}_y, \hat{\sigma}_z] = [24\text{ nm}, 28\text{ nm}, 42\text{ nm}]$. Hence we conclude that our approximation should only slightly overestimate localization error by a couple nanometers at most.

We applied Equation 1 to the time-ensemble averaged MSDs of each of our conditions individually to produce the average localization error estimates given in Table S2. It has been noted previously that the behavior of the DH-PSF is such that one can expect slightly worse precision in *y* than in *x* due to the oblong nature of the PSF, while precision in *z* is in turn worse than in either *x* or *y* (Badieirostami *et al.*, 2010).

	DLDC-dextrose	DLDC-galactose	*GAL/PES4*	*GAL/RPL9A*-dextrose	*GAL/RPL9A*-galactose	DLSC-30 kbp	DLSC-108 kbp	GFP crosstalk
$[\hat{\sigma}_x, \hat{\sigma}_y, \hat{\sigma}_z]$ (green)	11, 11, 17	13, 11, 27	13, 12, 22	14, 13, 22	14, 14, 29	13, 13, 23	14, 14, 30	11, 11, 19
$[\hat{\sigma}_x, \hat{\sigma}_y, \hat{\sigma}_z]$ (red)	23, 25, 38	23, 27, 47	24, 29, 40	28, 32, 57	27, 34, 60	24, 28, 45	21, 25, 41	22, 27, 40

Table S2 Localization precisions estimated from Equation 1 for each condition. All units are nanometers.

D. Unscaled velocity cross-correlations

If we do not wish to scale our definition of velocity correlations by the MSD we can define an alternative metric given by Equation S1:

$$\tilde{C}_{v_x}^{(g,r)}(\delta,\tau) = \delta^2 \left\langle v_{x,g}{}^{(\delta)}(t_{i_n}) v_{x,r}{}^{(\delta)}(t_{i_n}+\tau) \right\rangle . \qquad \text{(S1)}$$

Analogous definitions hold in *y* and *z*. We define the total value $\tilde{C}_v^{(g,r)}$ as the sum of the values for each dimension. The expected value of this metric is not affected by localization error. $\tilde{C}_v^{(g,r)}$ is plotted as a function of τ for various δ in Figure S3.

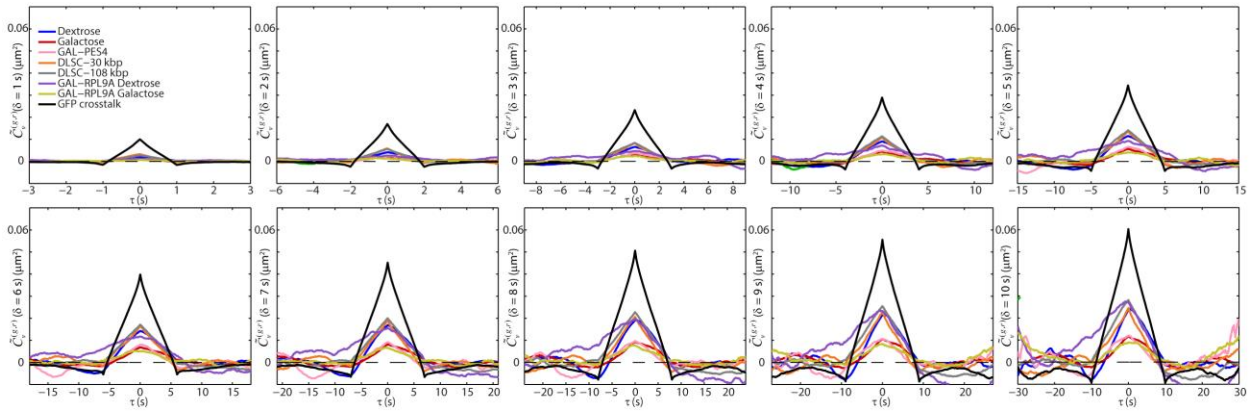

Figure S3 Time-ensemble averaged $\tilde{C}_v^{(g,r)}$ as a function of lag τ for all $\delta \in \{1s, 2s, 3s, 4s, 5s, 6s, 7s, 8s, 9s, 10s\}$.

The general relationships among the conditions are the same as they are for $C_v^{(g,r)}$, except that the *GAL/RPL9A*-dextrose case appears to join the ranks of DLDC-dextrose and the two DLSC cases. This fact highlights the importance of scaling away the MSD in the main text since the motions of these two unrelated loci appear otherwise correlated due to the observation of two

very high MSDs in this case (Figure S9). Again, the most notable data occur at $\tau = 0$, where the definition of $\tilde{C}_v^{(g,r)}$ is such that its value here becomes a sort of "cross MSD" (CMSD). We plot these values as a function of δ in Figure S4A. In Figure S4B we separate the DLDC-dextrose values into the three constituent sets and the DLDC-galactose values into the two constituent sets, in order to depict the level of repeatability.

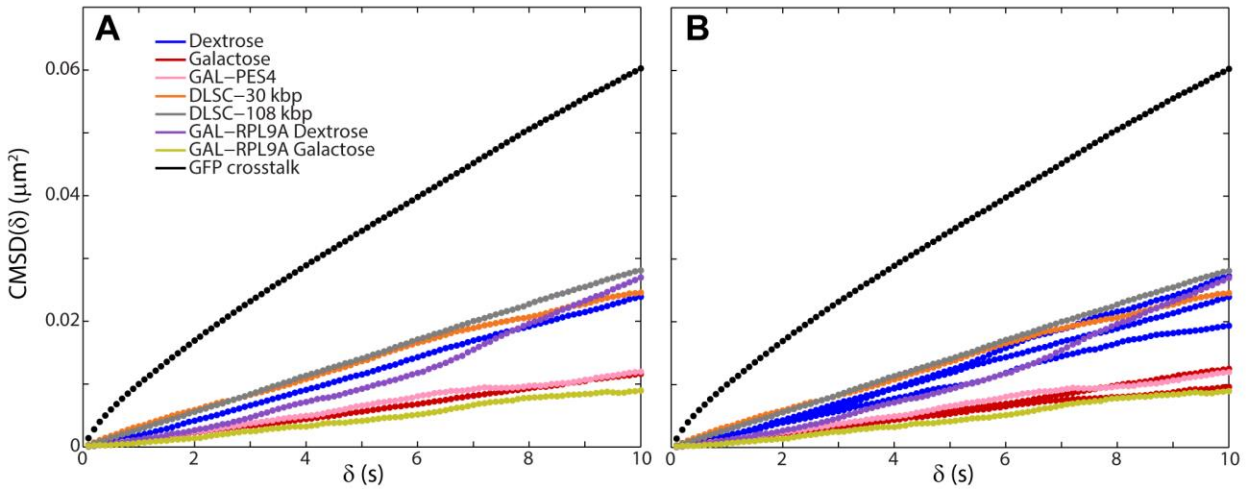

Figure S4 Time-ensemble averaged $\tilde{C}_v^{(g,r)}$ at $\tau = 0$, i.e. the CMSD, as a function of δ, (A) without and (B) with DLDC-dextrose and –galactose broken up into their constituent subsets. Data at integer values of δ are same data as center peaks in Figure S3.

E. Supplemental velocity cross-correlation plots

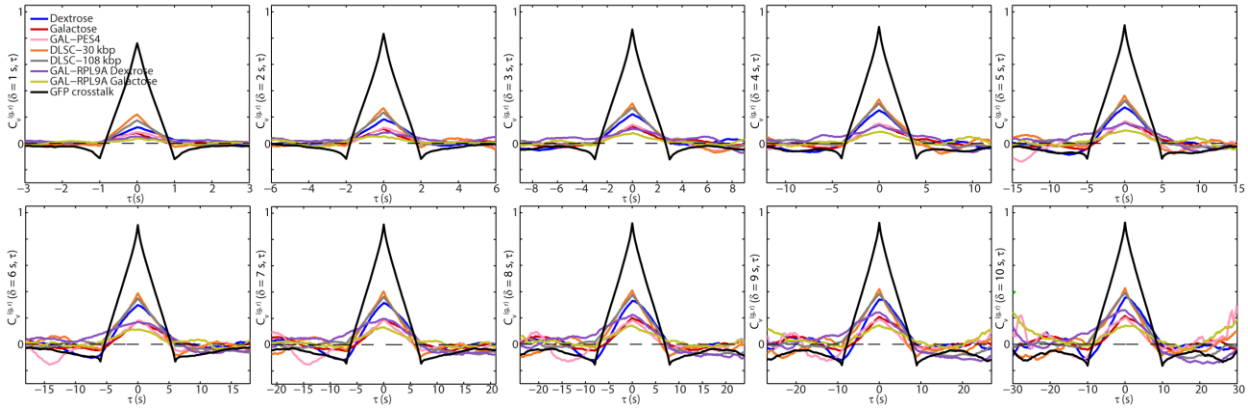

Figure S5 Time-ensemble averaged velocity cross-correlations as a function of lag τ for all $\delta \in \{1s, 2s, 3s, 4s, 5s, 6s, 7s, 8s, 9s, 10s\}$. The plots corresponding to δ = 1s and δ = 5 s appear in the main text.

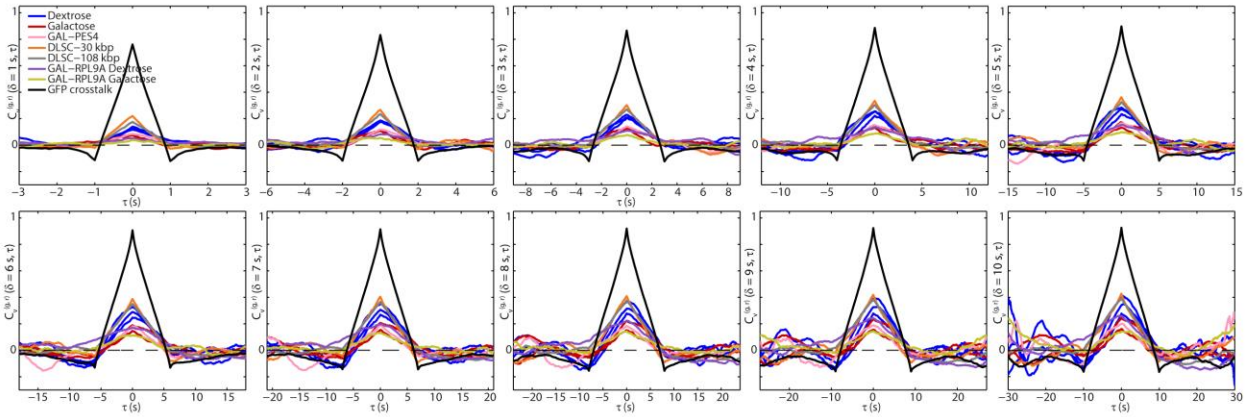

Figure S6 Same as Figure S5 except DLDC-dextrose is split into its three constituent sets and DLDC-galactose is split into its two constituent sets.

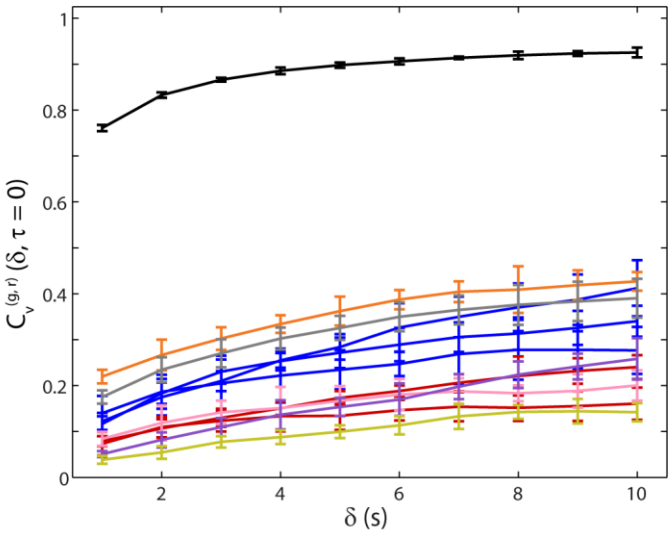

Figure S7 Time-ensemble averaged velocity cross-correlation at $\tau = 0$ as a function of $\delta \in \{1s, 2s, 3s, 4s, 5s, 6s, 7s, 8s, 9s, 10s\}$, with DLDC-dextrose and –galactose broken up into their constituent subsets. Same data as center peaks in Figure S6. Error bars are SEM.

F. Simulating effects of localization precision on $C_v^{(g,r)}$

As mentioned in the main text, the definition of $C_v^{(g,r)}$ given by Equation 3 means that higher localization error will cause a deflated estimation of $C_v^{(g,r)}$ that will increase with increasing δ, eventually asymptotically approaching the noiseless value. We quantified this effect by simulating coupled fBm between two particles as described elsewhere in the Supporting

Material, adding localization error, and calculating $C_v^{(g,r)}$. We simulated three cases with experimental parameters similar to those found for the crosstalk, DLDC-dextrose, and DLDC-galactose cases. In the crosstalk-inspired case we simulated a track of 500 steps, duplicated it, added localization error with standard deviation given by the appropriate entry in Table S2 (the "green" values to one copy of the track and "red" values to the duplicate), then repeated for a total of 1000 tracks. For the other cases we defined an appropriate correlation factor γ (see simulation section for definition. We used $\gamma = 0.35$ for the DLDC-dextrose-inspired case, and $\gamma = 0.2$ for the DLDC-galactose-inspired case.), then added localization error with standard deviations corresponding to the DLDC-dextrose or DLDC-galactose entries in Table S2. Again these were done for 1000 track pairs of 500 steps each. Figure S8 shows the results of this simulation. Note that the crosstalk-inspired simulation curve replicates the behavior of the experimental curve almost exactly, increasing from just below 0.8 at $\delta = 1$ s to just above 0.9 at $\delta = 10$ s. Thus the shape of the experimental crosstalk curve can be explained by the effects of localization error alone. For the other three simulated cases we see that there is a slight increase with increasing δ, but that the values at low δ are significantly higher than the corresponding experimental values. This discrepancy might be an indicator that the true form of the correlations is not consistent with the simple form assumed in the covariance matrix Γ (see simulation section), and that the true (noiseless) correlations may in fact themselves be increasing functions of δ. This might make sense if one thinks of two loci along separate chromosomes which are intertwined at some contact point away from the loci. For sufficiently low δ the motions of one locus will not be large enough to be felt by the other locus through the contact. For sufficiently large δ the motions will be larger than the distance to the contact and thus the motion between loci will be correlated.

We also simulated a set of track pairs with $\gamma = 0.35$ as in the DLDC-dextrose-inspired case, but with localization precision used in the DLDC-galactose-inspired case. The results are given by the dashed line in Figure S8. The dashed line is somewhat lower than the solid blue line, but significantly higher still than the red line, indicating that localization precision alone likely cannot explain the difference between correlations exhibited in the DLDC-dextrose and DLDC-galactose cases.

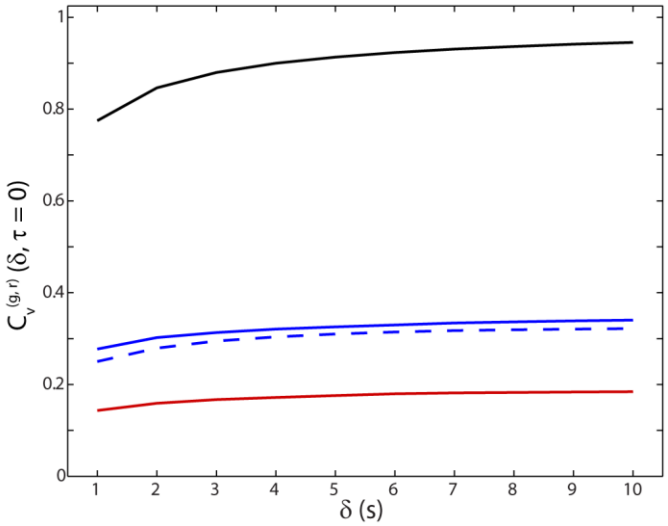

Figure S8 Time-ensemble averaged velocity cross-correlation at $\tau = 0$ as a function of $\delta \in \{1s, 2s, 3s, 4s, 5s, 6s, 7s, 8s, 9s, 10s\}$, for crosstalk-inspired (black), DLDC-dextrose-inspired (solid blue), and DLDC-galactose-inspired (red) simulations. Also shown is the result from a simulation with noiseless correlation inspired by the DLDC-dextrose case, but localization error consistent with DLDC-galactose (dashed blue).

G. Summary of all MSDs

Figure S9 shows the time-ensemble averaged MSDs in both channels across all conditions we studied. Figure S9A shows the MSDs on a linear scale as calculated in the green channel, while Figure S9B shows the same but for the red channel. In comparing the two, it seems that there is generally more heterogeneity between conditions in the green than in the red, save for the *GAL/RPL9A*-dextrose case in which the average may be skewed by an outlier with a particularly high MSD. This is reasonable since the red label was inserted at the same position near the *GAL* locus in all experiments, while the position of the green label was varied. In particular, we see that the green label in the DLSC cases are near the extremes of the cases along with DLDC-galactose, which itself was subject to unique conditions that affect its motion directly. Log-log plots that were used for estimation of subdiffusion parameters are shown in Figure S9C for the green channel and Figure S9D for the red channel. At early times there is a discernable upward bend due to the effects of localization error. This is especially apparent in the red channel, in which the localization error was about twice as large as that in the green. At long times the log-log MSD curves deviate from linearity due to poorer averaging. In the green channel there may be a preference to bend downward at these longer times, however, perhaps indicating the onset

of confinement. The log-log MSD curves were fit to a straight line over the intermediate interval [1 s, 10 s] to produce the fit parameters presented in Table S3. Note that the localization error is sufficiently high in the red channel as to deflate estimates of α even over the intermediate time interval. That this effect is indeed a consequence of poorer localization precision and not a labeling artifact is supported by the fact that it is evident in even the GFP crosstalk condition, which lacked the TetO/TetR-mCherry label.

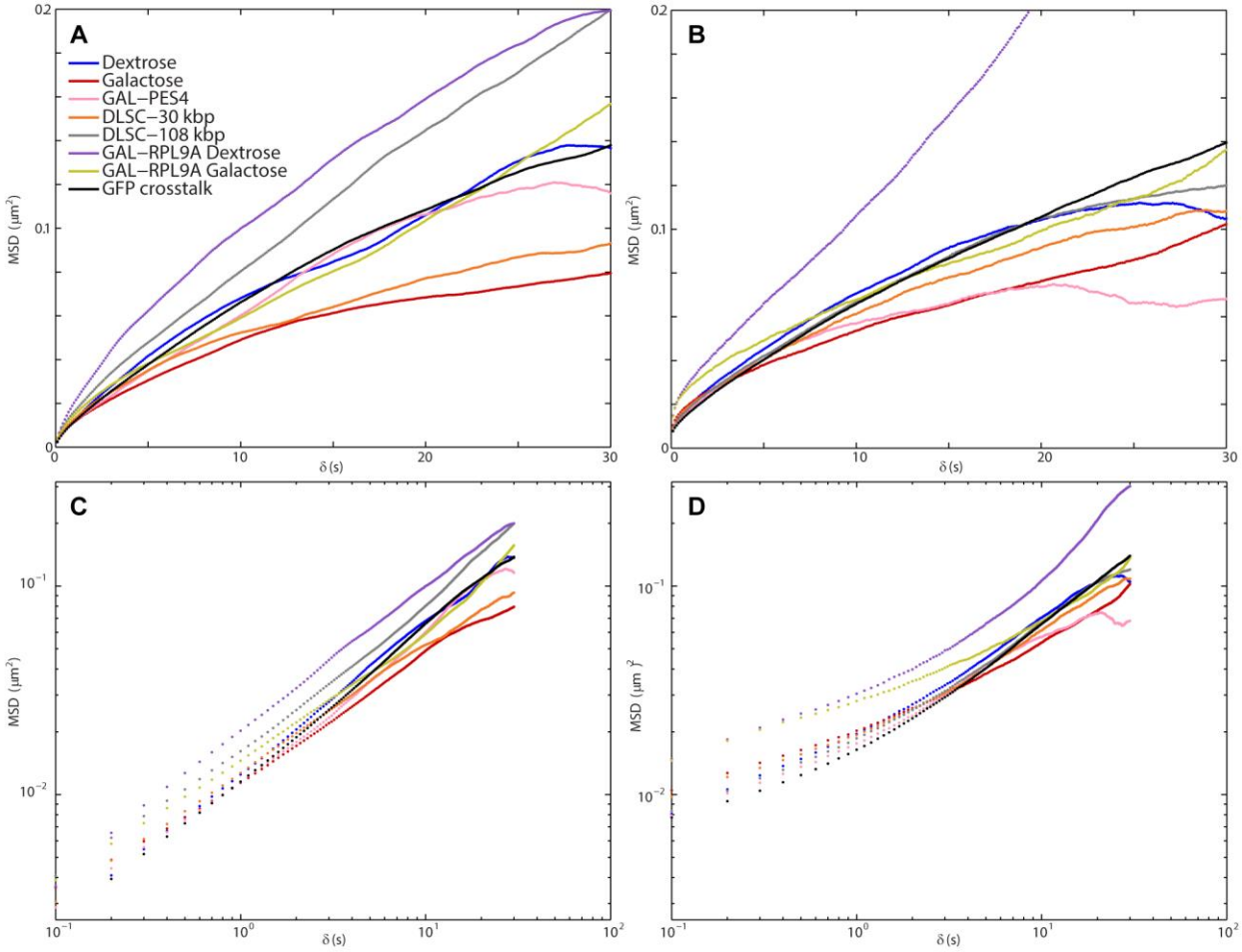

Figure S9 Time-ensemble averaged MSD curves across all conditions studied. (A) MSDs from green channel shown on a linear scale. (B) MSDs from red channel shown on linear scale. (C) MSDs from green channel shown on log-log scale. (D) MSDs from red channel shown on log-log scale.

	DLDC-dextrose	DLDC-galactose	*GAL/PES4*	*GAL/RPL9A*-dextrose	*GAL/RPL9A*-galactose	DLSC-30 kbp	DLSC-108 kbp	GFP crosstalk
$\hat{\alpha}_{green}$	0.75	0.64	0.73	0.70	0.60	0.62	0.70	0.77
$\hat{D}^*_{green}$	0.0020	0.0018	0.0018	0.0034	0.0024	0.0021	0.0026	0.0018
$\hat{\alpha}_{red}$	0.58	0.43	0.55	0.57	0.40	0.53	0.58	0.63
$\hat{D}^*_{red}$	0.0030	0.0032	0.0028	0.0045	0.0044	0.0030	0.0028	0.0025

Table S3 Estimated subdiffusion parameters over the time interval [1 s, 10 s].

H. MSD without overlapping intervals

When computing the MSD for $\delta > \delta_{\min}$ one has a choice as to whether to use overlapping frame intervals or not. Allowing overlapping intervals, as done throughout this study, reduces scatter in the resulting curve due to averaging of a larger population of displacements at each δ. However, overlapping intervals are not statistically independent and so the resulting computed MSD curve can be biased if the tracks themselves are not long enough or if there are too few tracks over which to average. To ensure that the subdiffusion parameters we estimated were not artifacts resulting from the use of overlapping intervals we calculated the MSDs from the green channel in each condition to produce the noisier curves shown in Figure S10. Fitting over the interval [1 s, 10 s] gives the parameter estimates given in Table S4. Clearly the values do not change appreciably relative to those presented in Table S3.

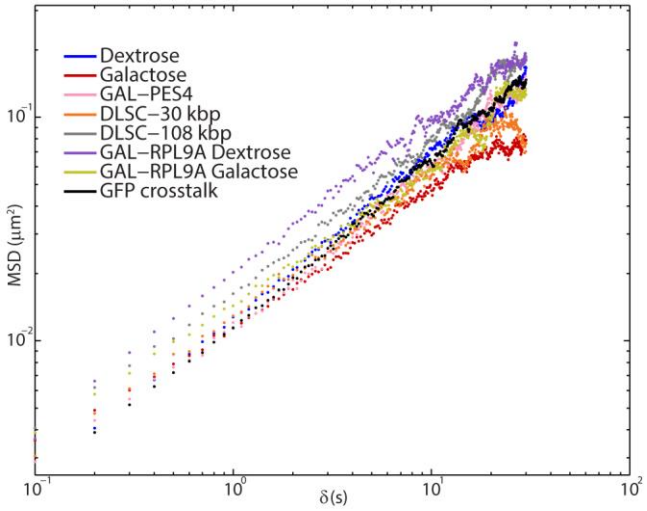

Figure S10 Computed MSDs of each condition from data in the green channel, without allowing for overlapping intervals.

	DLDC-dextrose	DLDC-galactose	*GAL/PES4*	*GAL/RPL9A*-dextrose	*GAL/RPL9A*-galactose	DLSC-30 kbp	DLSC-108 kbp	GFP crosstalk
$\hat{\alpha}_{green}$	0.76	0.64	0.76	0.68	0.61	0.64	0.68	0.78
$\hat{D}^{*}_{green}$	0.0021	0.0018	0.0018	0.0034	0.0024	0.0021	0.0027	0.0018

Table S4 Estimated subdiffusion parameters over the time interval [1 s, 10 s], without allowing for overlapping intervals in MSD.

I. Relative MSD

We also calculated the relative MSD, MSD_{rel}, defined according to Equation S2:

$$MSD_{rel}(\delta) = \left\langle \left| \left(\vec{r}_g(t_{i_n} + \delta) - \vec{r}_r(t_{i_n} + \delta) \right) - \left(\vec{r}_g(t_{i_n}) - \vec{r}_r(t_{i_n}) \right) \right|^2 \right\rangle, \quad \text{(S2)}$$

where the subscript "g" denotes position measured in the green channel and "r" denotes red. Note that MSD_{rel} essentially removes the correlations from the normal MSD. In fact, one can show with some algebra that

$$MSD_{rel}(\delta) = MSD_g(\delta) + MSD_r(\delta) - 2CMSD(\delta). \quad \text{(S3)}$$

Thus the quantity MSD_{rel} includes the same information as the combined MSDs (Figure S9) and CMSD (Figure S4). Nonetheless, we plot MSD_{rel} in Figure S11A. For comparison, the quantity on the RHS of Equation S3 is plotted in Figure S11B. The slight differences in the plots are due to statistical errors caused by the order of averaging. With the correlations essentially removed, MSD_{rel} values are determined by the MSDs of the individual loci themselves and the distribution of inter-locus distances for each pair.

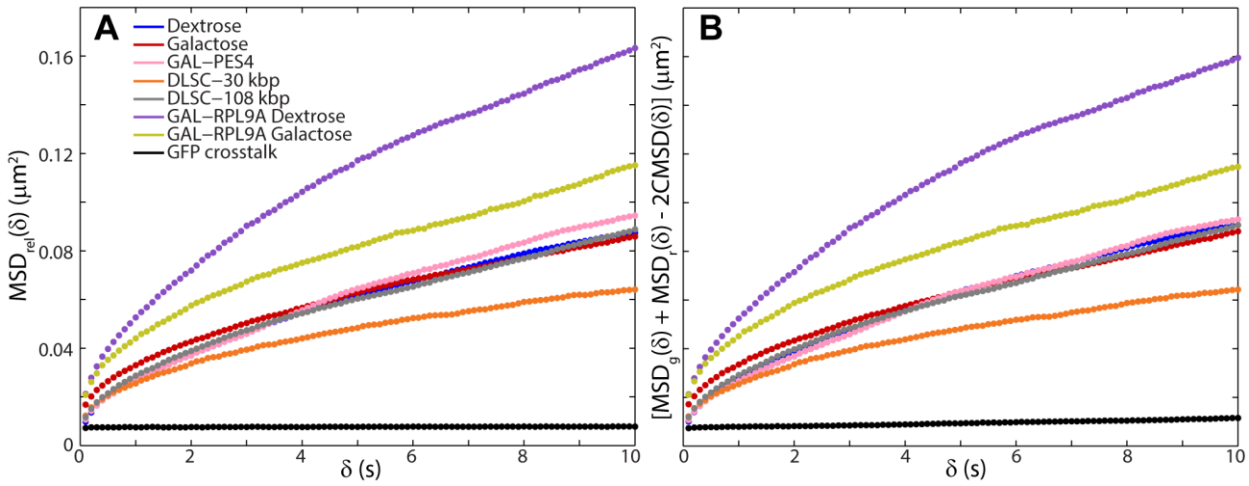

Figure S11 Relative MSDs. (A) MSD_{rel} as defined in Equation S2. (B) Statistically equivalent quantity occurring in the RHS of Equation S3.

J. Control experiment: tracking beads in glycerol mixture

In light of the surprising subdiffusive scaling exponent we found for the DNA loci we conducted a control experiment in which we tracked fluorescent beads in a glycerol/water mixture. These beads should undergo pure diffusion, and so our analysis should recover $\alpha = 1$. In order to control for sample drift as we did in the locus tracking experiments, we first immobilized an amount of 200 nm red fluorescent beads (FluoSpheres, Invitrogen, Carlsbad, CA) at the coverslip by diluting by 500 from stock into 1% polyvinyl alcohol (Polysciences, Inc., Warrington, PA) solution and spincoating. Two additional spincoating layers of PVA solution were added on top of this in an attempt to protect the immobilized beads from escaping into solution during imaging. These samples were left to air dry for 1 week before imaging. Another portion of 200 nm red fluorescent beads was diluted by 10^4 from stock into a 90% (by weight) glycerol/water mixture. An aliquot of this solution was placed on top of a sample containing beads immobilized at the surface for imaging. Imaging was done on the same setup as the locus tracking. We excited with the same 561 nm laser described in the Materials and Methods section and imaged through the same filter set. Images were only recorded in the red channel. Appropriate fields of view for analysis contained at least one immobilized bead within the same depth of focus as at least one bead moving in solution. This proved somewhat rare, possibly as a result of the glycerol mixture leaching the PVA matrix and sucking immobilized beads into solution. Still we were able to collect data from 11 3D tracks which lasted for ~82 s on average. The relatively long track

lengths provided sufficient statistics for MSD analysis despite the relatively low number of tracks. Figure S12A shows the resulting time-ensemble averaged MSD over the time range [1 s, 10 s], along with the linear fit. The fit yielded estimated parameters of $D^* = 0.011$ and $\alpha = 0.98$. Thus indeed we find sound agreement with the expected $\alpha = 1$. The estimated diffusion coefficient is in reasonable agreement with that predicted from the Stokes-Einstein relation. Figure S12B depicts the scaled velocity autocorrelation as in Figure 6 in the main text. The data shown is only for δ on the interval [1 s, 5 s] since reduced averaging made data for $\delta > 5$ s unreliable. Fitting to Equation 6 from the main text gave $\alpha = 0.97$. The lack of negative-going peak at $\tau/\delta = 1$ is indicative of pure Brownian motion.

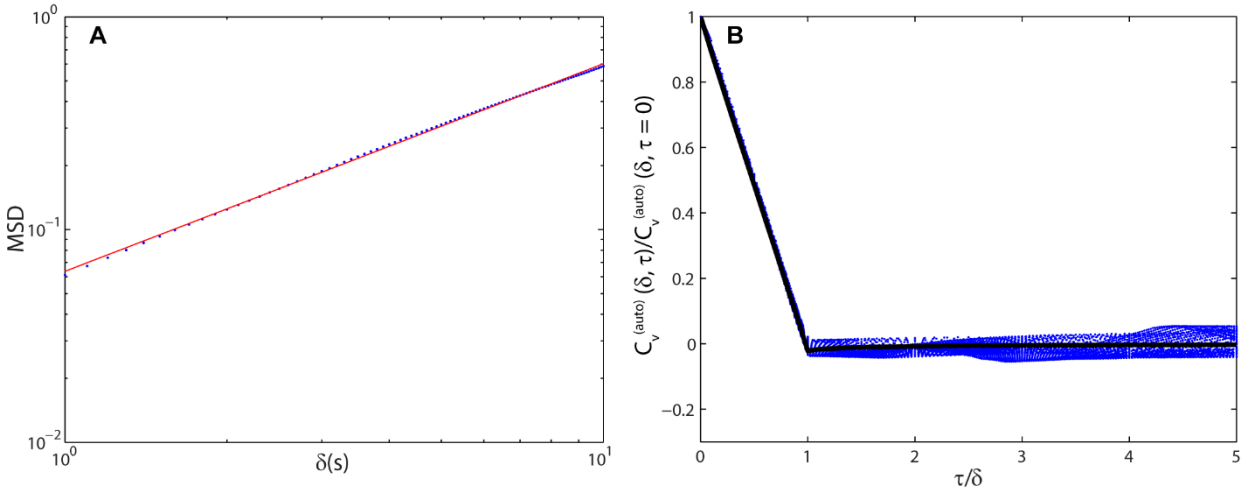

Figure S12 Results of tracking fluorescent beads in glycerol/water mixture. (A) MSD (blue dots) calculated from data along with linear fit (red line) to log-log plot. (B) Scaled velocity autocorrelation as defined in Equation 5 in the main text. Data for δ on the interval [1 s, 5 s] is included. Fit to Equation 6 with free parameter α (black line).

K. Upper bound of contribution of nuclear translation to MSD

Some previous studies (usually taking place over longer time periods) have taken measures to remove nuclear translation from the apparent translation of chromosomal loci by staining the nucleus or nuclear periphery in a separate color and subtracting the centroid of the nuclear fluorescence signal from that of the locus signal (Marshall *et al.*, 1997; Cabal *et al.*, 2006; Sage, 2005). The underlying equation employed is:

$$\vec{v}^{(\delta)}(t) = \vec{v}_L{}^{(\delta)}(t) - \vec{v}_N{}^{(\delta)}(t), \qquad \text{(S4)}$$

where $\vec{v}^{(\delta)}(t)$ is the velocity of the locus in nuclear coordinates, $\vec{v}_L{}^{(\delta)}(t)$ is the apparent velocity of the locus in lab coordinates, and $\vec{v}_N{}^{(\delta)}(t)$ is the velocity of the nucleus. In the current study we

did not label the nucleus in a third color and so we could not directly remove the contribution from nuclear translation to the overall motion. However, we can provide an upper bound for the contribution of nuclear translation to the overall MSD by using simultaneous locus data from the two color channels. By rearranging Equation S4 and using the subscripts "g" and "r" to refer to the green and red channels, we get

$$\begin{aligned}\vec{v}_{L,g}{}^{(\delta)}(t) &= \vec{v}_g{}^{(\delta)}(t) + \vec{v}_N{}^{(\delta)}(t) \\ \vec{v}_{L,r}{}^{(\delta)}(t) &= \vec{v}_r{}^{(\delta)}(t) + \vec{v}_N{}^{(\delta)}(t)\end{aligned}. \quad \text{(S5)}$$

Using these two expressions we find

$$\begin{aligned}\left\langle \vec{v}_{L,g}{}^{(\delta)}(t)\cdot\vec{v}_{L,r}{}^{(\delta)}(t)\right\rangle = \quad & \left\langle \vec{v}_g{}^{(\delta)}(t)\cdot\vec{v}_r{}^{(\delta)}(t)\right\rangle + \left\langle \vec{v}_g{}^{(\delta)}(t)\cdot\vec{v}_N{}^{(\delta)}(t)\right\rangle \\ & + \left\langle \vec{v}_r{}^{(\delta)}(t)\cdot\vec{v}_N{}^{(\delta)}(t)\right\rangle + \left\langle \vec{v}_N{}^{(\delta)}(t)\cdot\vec{v}_N{}^{(\delta)}(t)\right\rangle\end{aligned}. \quad \text{(S6)}$$

The second and third terms in the right hand side of Equation S6 evaluate to zero. The last term in the right hand side of Equation S6 is proportional to the MSD of the nucleus over the time δ, which we can denote $MSD_N(\delta)$. Thus Equation S6 becomes

$$\left\langle \vec{v}_{L,g}{}^{(\delta)}(t)\cdot\vec{v}_{L,r}{}^{(\delta)}(t)\right\rangle = \left\langle \vec{v}_g{}^{(\delta)}(t)\cdot\vec{v}_r{}^{(\delta)}(t)\right\rangle + \frac{1}{\delta^2}MSD_N(\delta). \quad \text{(S7)}$$

Rearranging Equation S7 then gives

$$MSD_N(\delta) = \delta^2\left\langle \vec{v}_{L,g}{}^{(\delta)}(t)\cdot\vec{v}_{L,r}{}^{(\delta)}(t)\right\rangle - \delta^2\left\langle \vec{v}_g{}^{(\delta)}(t)\cdot\vec{v}_r{}^{(\delta)}(t)\right\rangle. \quad \text{(S8)}$$

The first term in the right hand side of Equation S8 can be calculated from the data acquired. The second term cannot be calculated from the data we have available. However, it is likely fair to assume that $\delta^2\left\langle \vec{v}_g{}^{(\delta)}(t)\cdot\vec{v}_r{}^{(\delta)}(t)\right\rangle$ must be positive since a negative value would likely correspond to an active pulling apart of the loci, as explained in the text. By this assumption we can provide a calculable upper bound to $MSD_N(\delta)$:

$$MSD_N(\delta) \le \delta^2\left\langle \vec{v}_{L,g}{}^{(\delta)}(t)\cdot\vec{v}_{L,r}{}^{(\delta)}(t)\right\rangle. \quad \text{(S9)}$$

Note that $\delta^2\left\langle \vec{v}_{L,g}{}^{(\delta)}(t)\cdot\vec{v}_{L,r}{}^{(\delta)}(t)\right\rangle = CMSD(\delta)$, where CMSD is the "cross MSD" that is plotted in Figure S4. Equation S9 was used to calculate the upper bounds for $MSD_N(\delta)$ in dextrose and galactose cases as plotted in Figure 6A in the main text. If we expand the apparent MSD as measured in the lab frame in a manner analogous to Equation S6, we easily find $MSD_L(\delta) = MSD(\delta) + MSD_N(\delta)$, i.e. the apparent MSD is the sum of the true MSD and the

nuclear MSD. Thus the uncorrected nuclear translation could inflate the apparent MSD and possibly cause incorrect estimations of α.

For this reason we subtracted the bounds of MSD_N derived from Equation (S7) and found that the estimated α values were only slightly depressed to 0.71 in dextrose and 0.57 in galactose. We also note that varying the shape of the MSD_N bound by varying its concavity subject to the constraint that it must be less than or equal to the global bound of Equation S9 did not seem to account for a massive difference in the apparent α. Namely we allowed for our MSD_N to take the form $k\delta^{\alpha'}$ where we chose various $\alpha' \in (0,2]$ and then chose constant $k = \arg\min\left\{\int\left|\delta^2\left\langle \vec{v}_{L,g}{}^{(\delta)}(t)\cdot\vec{v}_{L,r}{}^{(\delta)}(t)\right\rangle - k\delta^{\alpha'}\right|^2 d\delta : \left[\delta^2\left\langle \vec{v}_{L,g}{}^{(\delta)}(t)\cdot\vec{v}_{L,r}{}^{(\delta)}(t)\right\rangle - k\delta^{\alpha'} > 0\right]\forall\delta\right\}$. This treatment only produced apparent α between 0.67 and 0.77 for the dextrose case, for instance. Finally, we considered the unlikely case that even within the same carbon source, the DLDC and *GAL/PES4* strains exhibited significantly different MSDN such that the *GAL/PES4* case is a bad bound for MSD_N in DLDC-dextrose. For this we used the CMSD of the DLDC-dextrose case itself as a bound and estimated α to be 0.63. Thus the effects of nuclear translation can likely be ruled out as a possible explanation for the apparent super-Rousean behavior of the loci.

L. Offset of MSD due to localization error

Finite localization precision σ is known to cause a constant offset in the linear MSD curve for pure Brownian motion according to Equation S10 (in one dimension) (Savin and Doyle, 2005):

$$MSD(\delta) = 2D\delta + 2\sigma^2. \qquad \text{(S10)}$$

However, localization error also causes a constant offset in the MSD for subdiffusive (or superdiffusive) motion, despite the fact that it is often ignored in this context. Here we give a derivation which shows this result is general. We restrict the derivation to one dimension, but extension to three dimensions is straightforward. Let $x(t_i)$ be the position at time t_i of the particle undergoing subdiffusive (or superdiffusive) motion and let $\xi(t_i)$ be a random Gaussian variable representing the localization error such that at time t_i. The estimated position of the particle (e.g. from fitting to a Gaussian and finding the mean) is given by the sum $x(t_i) + \xi(t_i)$. Let $\xi(t)$ be a stationary process with mean zero and covariance function given by:

$$\left\langle \xi(t_1)\xi(t_2)\right\rangle = \begin{cases}\sigma^2, t_1 = t_2\\ 0, t_1 \neq t_2\end{cases}. \qquad \text{(S11)}$$

In real particle tracking experiments $\xi(t)$ may not be stationary due to photobleaching but this is an additional complication that is not considered here. The MSD can be computed:

$$MSD(\delta) = \left\langle \left(x(t_i + \delta) + \xi(t_i + \delta) - x(t_i) - \xi(t_i) \right)^2 \right\rangle. \quad \text{(S12)}$$

Since $x(t)$ and $\xi(t)$ are independent we have

$$MSD(\delta) = \left\langle \left(x(t_i + \delta) - x(t_i) \right)^2 \right\rangle + \left\langle \left(\xi(t_i + \delta) - \xi(t_i) \right)^2 \right\rangle. \quad \text{(S13)}$$

The term on the left is equal to $2D\delta^\alpha$ by construction, while the term on the right is equal to $2\sigma^2$ by Equation S11. Thus we conclude

$$MSD(\delta) = 2D\delta^\alpha + 2\sigma^2, \quad \text{(S14)}$$

and so indeed we see that we obtain the MSD curve expected in the absence of localization noise plus a constant offset, regardless of the value of α.

M. Simulating fractional Brownian motion

To simulate fBm one can generate *x*, *y*, and z velocities at discrete time steps t_i separated by $\delta_{\min}$ such that $v_x(t_i)$, $v_y(t_i)$, $v_z(t_i)$ are mean-zero Gaussian processes satisfying the following covariance relation (Dieker, 2004):

$$\left\langle v_x(t_i) v_x(t_j) \right\rangle = D^* \delta_{\min}^{\alpha-2} \left[\left(\frac{|t_j - t_i|}{\delta_{\min}} + 1 \right)^\alpha - 2 \left(\frac{|t_j - t_i|}{\delta_{\min}} \right)^\alpha + \left| 1 - \frac{|t_j - t_i|}{\delta_{\min}} \right|^\alpha \right]. \quad \text{(S15)}$$

Equation S15 is a rearranged version of Equation 6 in the main text, and analogous equations hold for v_y and v_z. Thus $v_x(t)$, $v_y(t)$, and $v_z(t)$ are each Gaussian random vectors with covariance matrix $\mathbf{\Sigma}$ with entries:

$$\Sigma_{ij} = D^* \delta_{\min}^{\alpha-2} \left[(|j - i| + 1)^\alpha - 2|j - i|^\alpha + |1 - |j - i||^\alpha \right]. \quad \text{(S16)}$$

There are several ways to generate a random vector with a specified covariance matrix $\mathbf{\Sigma}$ in MATLAB. The simplest way is to use the built-in function `mvnrnd`.

N. Simulating correlated fractional Brownian motions

For some of our simulations we wanted to look at two particles undergoing fBm which were correlated with one another, so as to imitate the correlated motions we saw in experiments. To do so we combined the two vectors of velocities corresponding to each particle's velocities into one

large vector $w_x = [v_{x,1};v_{x,2}]$ (likewise for y and z) and defined the covariance matrix Γ for the whole coupled system as a collection of block matrices:

$$\Gamma = \begin{bmatrix} \Gamma_{11} & \Gamma_{12} \\ \Gamma_{21} & \Gamma_{22} \end{bmatrix}, \qquad \text{(S17)}$$

where Γ_{11} contains the correlations of velocities of only particle 1 and has the form given by Equation S16, Γ_{22} is the same as Γ_{11} but pertaining to particle 2, and $\Gamma_{12} = \Gamma_{21}$ contains the information about correlations between the particles. Note that implicit in this treatment of correlated motions is the assumption that $v_{x,1}$ and $v_{x,2}$ are jointly Gaussian, which may not be the case in reality. A more rigorous treatment would be to solve the Langevin equation which includes a term describing the coupling forces between the particles. However, approximation as a jointly Gaussian process is a useful simplification. The form of Γ_{12} should be prescribed by our experimental findings for $C_v^{(g,r)}$. However, the effects of localization error and finite statistics make it dubious to equate them directly. Thus we considered a few ways to define Γ_{12} that would give the expected TEAVCC. The simplest way would be to make the diagonal of Γ_{12} equal to a constant between 0 and 1 (proportional to $C_v^{(g,r)}$) and all other entries 0. However, the resulting Γ would not be a covariance matrix of a Gaussian process since it would not be positive semidefinite. A simple way to create a positive semidefinite Γ that we found was to equate $\Gamma_{12} = \gamma\Gamma_{11}$, where $0<\gamma<1$ is a constant related to $C_v^{(g,r)}$. Thus we chose to simulate our coupled fBm in this fashion. However, it is worth noting that this cannot exactly describe the motion we observed in experiments since we noted that the TAVCC of individual track pairs did not have the same shape as the TEAVCC, as the former often showed peaks away from $\tau = 0$. Again, a more exact but complicated description would invoke the appropriate Langevin equation.

O. Simulating confined fractional Brownian motion

For some of our simulations we confined the particle undergoing fBm within a finite radius. Thus we had to modify the method of simulation detailed in the above section to allow us to generate $\vec{v}(t_i)$ in each step individually, then redraw if this step would result in leaving the radius of confinement. To generate each step individually we invoked the probability distribution of $v_x(t_i)$ given its values at $t_1,\ldots t_{i-1}$. This is a Gaussian random variable with mean μ and variance σ^2

related to the matrix **Σ** defined in Equation S16 and the values $v_x(t_1),\ldots,v_x(t_{i-1})$, which we denote collectively as the vector $\vec{v}_x^{\,i-1}$. μ is given by Equation S18:

$$\mu = \Sigma_{12}\Sigma_{22}^{-1}\vec{v}_x^{\,i-1}, \qquad \text{(S18)}$$

and σ^2 is given by Equation S19:

$$\sigma^2 = \Sigma_{11} - \Sigma_{12}\Sigma_{22}^{-1}\Sigma_{21}. \quad \text{(S19)}$$

Σ_{11}, Σ_{12}, Σ_{21}, and Σ_{22} are defined in Equation S20:

$$\begin{aligned}
&\Sigma_{11} = 2D^*\delta_{\min}^{\alpha} \\
&\Sigma_{12} = [\Sigma_{i,i-1},\ldots,\Sigma_{i,1}] \\
&\Sigma_{21} = \Sigma_{12}^{\,T} \\
&\{\Sigma_{22}\}_{i',j'} = \Sigma_{i-i',j-j'},\ \forall i',\ j' \in \{1,\ldots,i-1\}
\end{aligned} \quad . \qquad \text{(S20)}$$

P. Simulations addressing deflated α estimates

In order to provide a possible explanation for the discrepancy between our findings for the value of α (~0.6-0.75) and those of previous studies (~0.4-0.5) for the *GAL* locus we simulated confined 3D fBm using the computational method described in the previous section with physically motivated parameters and measurement parameters consistent with those of reference (Cabal *et al.*, 2006). We used α = 0.75 and D^* = 0.0021, based on our experimental values. The radius of confinement was set to 0.5 μm, consistent with the size of the gene territory of the *GAL* locus in dextrose found in reference (Berger *et al.*, 2008). We simulated 10 tracks each of length 900 s with frame intervals of 4 s, consistent with reference (Cabal *et al.*, 2006). Random localization error was added to each track such that the total standard deviation of the error was $\sigma = \sqrt{\sigma_x^{\,2} + \sigma_y^{\,2} + \sigma_z^{\,2}} = 60\,\text{nm}$, also according the reported value in reference (Cabal *et al.*, 2006). From the resulting tracks we calculated the time-ensemble averaged MSD(δ) and fit the first 22 points [i.e. the first <90 s as in (Cabal *et al.*, 2006)] to a curve of the form $\hat{D}^*\delta^{\hat{\alpha}}$, where the hats denote free parameters to be estimated. Repeating over 10 trials yielded estimated parameters of $\hat{D}^* = 0.025 \pm 0.002$ and $\hat{\alpha} = 0.47 \pm 0.02$ (error is standard deviation). This is in very close agreement with the reported parameters in reference (Cabal *et al.*, 2006) in glucose of $\hat{D}^* = 0.024$ and $\hat{\alpha} = 0.43$. Figure S13 depicts the MSD curve and fit in both linear (Figure S13A) and log-log (Figure S13B) scale for one particular trial in which we estimated the parameters to

be $\hat{C} = 0.027$ and $\hat{\alpha} = 0.46$. The qualitative agreement between the fit and the data is admittedly not as strong as that shown in reference (Cabal *et al.*, 2006). Increasing the standard deviation of the localization error by a factor of $\sqrt{3}$ in each direction (e.g. in case the reported estimate of localization error was too low) improves the agreement with the fit, as shown in Figure S13, C and D for one particular example trial which yielded estimates of $\hat{D}^* = 0.031$ and $\hat{\alpha} = 0.44$. We also reiterate here that preliminary data suggest a relation between background strain and character of motion that needs to be more fully elucidated.

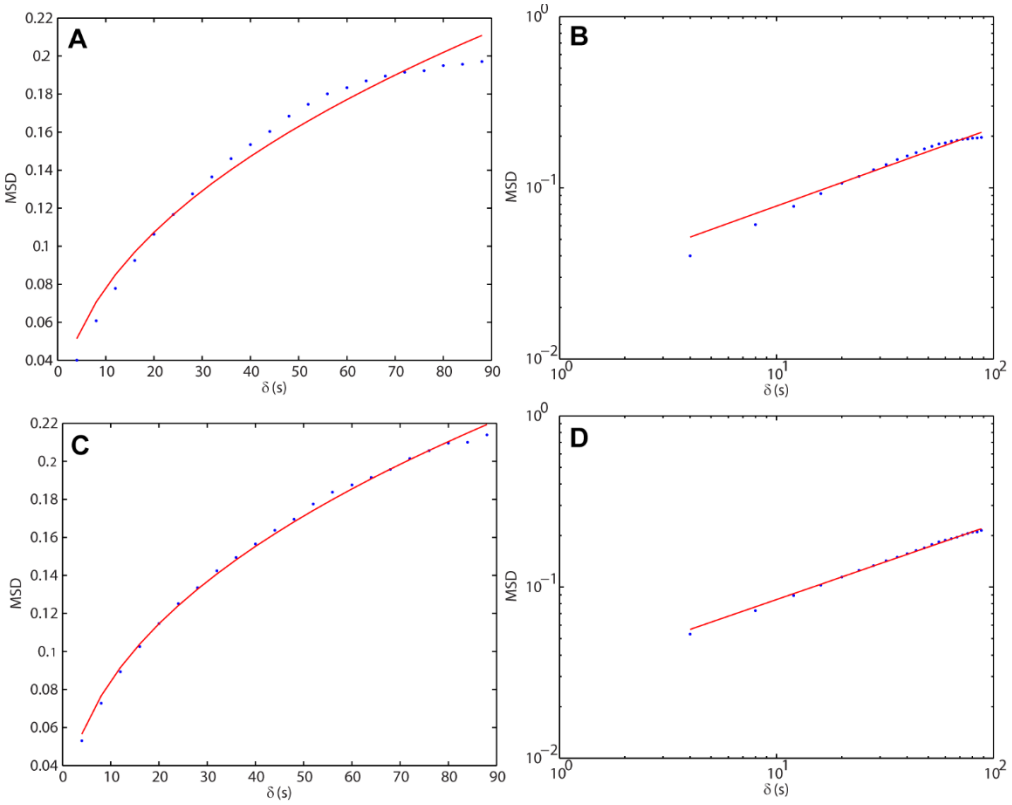

Figure S13 Results of one trial of simulated confined 3D fBm using the parameters described in the text, with lower localization error (A and B) and higher localization error (C and D).

Q. Example track pair movies

Movies S1-S5 show the fit trajectories of the green and red loci for 5 example track pairs coming from various conditions. Playback is in real time. The bottom right panel of each movie shows the inter-locus distance as a function of time, while the other three panels show the *x*-*y*, *x*-*z*, and *y*-*z* projections of the positions of both loci in each frame.

Movie S1 An example from the GFP crosstalk condition showing correlations near unity.

Movie S2 A fairly highly correlated example from the DLDC-dextrose condition, despite large inter-locus separation.

Movie S3 An example from the DLDC-galactose condition showing low average correlations.

Movie S4 An example from the GAL/PES4 case showing low average correlations.

The time-averaged velocity correlations of each of the examples depicted in Movies S1-S5 are shown in Figure S14. Note that the peak of the DLDC-dextrose example occurs at $\tau < 0$, in contrast to the example given in Figure 5 in the main text. This indicates that the green locus tends to lead the red locus in this particular pair.

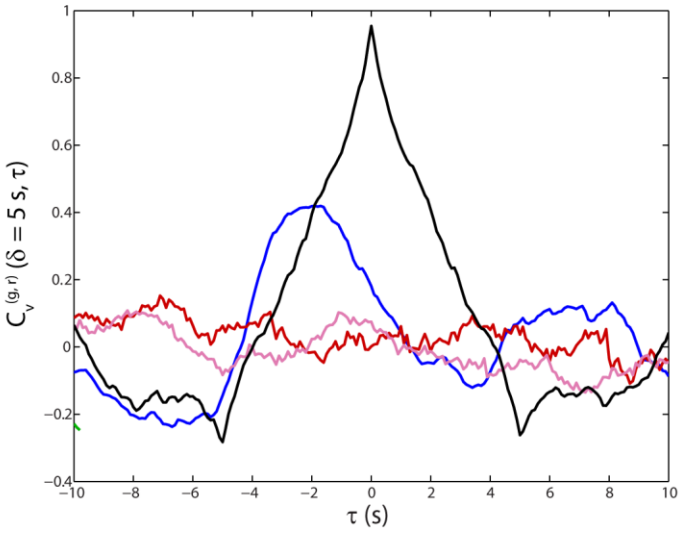

Figure S14 Time-averaged velocity cross-correlation for example track pairs depicted in Movies S1-S4, taken from the crosstalk condition (black), DLDC-dextrose (blue), DLDC-galactose (red), and *GAL/PES4* (pink).

R. Examples of apparently peripheral track pairs

As mentioned in the main text, a number of tracks appeared to trace out a portion of the nuclear periphery, as has been shown previously to occur, especially in galactose (Cabal *et al.*, 2006). Figure S15-S17 are MATLAB .fig files showing the 3D trajectories from three such examples from the DLDC-galactose condition. These figures can be rotated in 3D to explore this apparent curvature. Figure S15 is the same track pair that was used for Figure 5, E-I, which shows the two loci are sequestered apart from one another. The TAVCC for this pair is -0.09 for $\delta = 5$ s and $\tau = 0$. Figure S16 and S17 show two example pairs in which the loci seem to occupy the same region of space. The TAVCC values for these pairs are correspondingly higher: 0.29 for the pair in S16 and 0.23 for that in S17.

References

Badieirostami, M., Lew, M. D., Thompson, M. A. and Moerner, W. E. (2010). Three-dimensional localization precision of the double-helix point spread function versus astigmatism and biplane. Appl. Phys. Lett. *16*, 161103.

Berger, A. B., Cabal, G. G., Fabre, E., Duong, T., Buc, H., Nehrbass, U., Olivo-Marin, J. C., Gadal, O. and Zimmer, C. (2008). High-resolution statistical mapping reveals gene territories in live yeast. Nat. Methods, 1031-1037.

Cabal, G. G., Genovesio, A., Rodriguez-Navarro, S., Zimmer, C., Gadal, O., Lesne, A., Buc, H., Feuerbach-Fournier, F., Olivo-Marin, J. and Hurt, E. D. (2006). SAGA interacting factors confine sub-diffusion of transcribed genes to the nuclear envelope. Nature, 770-773.

Dieker, T. (2004). Simulation of fractional Brownian motion. MSc theses, University of Twente, Amsterdam, The Netherlands.

Hirsch, M., Wareham, R. J., Martin-Fernandez, M. L., Hobson, M. P. and Rolfe, D. J. (2013). A stochastic model for electron multiplication charge-coupled devices–from theory to practice. PloS one *1*, e53671.

Marshall, W. F., Straight, A., Marko, J. F., Swedlow, J., Dernburg, A., Belmont, A., Murray, A. W., Agard, D. A. and Sedat, J. W. (1997). Interphase chromosomes undergo constrained diffusional motion in living cells. Curr. Biol., 930--939.

Sage, D. (2005). Automatic Tracking of Individual Fluorescence Particles: Application to the Study of Chromosome Dynamics. IEEE Trans. Image Processing *9*, 1372-1383.

Savin, T. and Doyle, P. S. (2005). Static and Dynamic Errors in Particle Tracking Microrheology *1*, 623-638.